



Ultra-wideband linear-polarization conversion metasurface with high-efficient asymmetric transmission

Xiaojun Huang¹ · Xiongwei Ma¹ · Huanhuan Gao¹ · Linyan Guo² · Xiaoyan Li³

Received: 3 October 2022 / Accepted: 24 February 2023 / Published online: 21 March 2023
© The Author(s), under exclusive licence to Springer-Verlag GmbH, DE part of Springer Nature 2023

Abstract

In this paper, we present an ultra-wideband linear-polarization converter with excellent efficient asymmetric transmission characteristics. Numerical simulations present that the polarization conversion ratio is greater than 0.9 at 4.6–14.0 GHz and its asymmetric transmission parameter reaches 0.7 at the same frequency region. The microwave experiment is performed to prove the simulations, and the experimental results coincide with the simulation results. The mechanisms of polarization conversion and asymmetric transmission are explained by distributions of surface current and electric field. The superposition of multiple resonances broadens the bandwidth. We believe that our work is of great significance to potential applications for manipulating electromagnetic waves.

Keywords Ultra-broadband · Polarizer · Asymmetric transmission · Metasurface

1 Introduction

Metasurface (MS) can be regarded as a two-dimensional metamaterial due to its ultrathin physical property, which has some unique physical characteristics by tweaking the geometric shape of the structure [1]. It has many practical

applications in polarization manipulation [2–4], vortex waves [5], abnormal reflection [6], and other application fields [7–10]. Polarization is a crucial property of electromagnetic (EM) waves, especially in the microwave or optical regimes, and manipulating the polarized states of EM waves flexibly and arbitrarily has wide applications in meta-lens [11], hologram [12], radio communication [13] and antennas engineering field [14]. Traditional methods to manipulate polarization states using birefringent crystal and diffraction grating suffer from the large volume and high loss [15]. Recently, the appearance of MS paves a new path in manipulating the polarized states of EM waves [16–18]. Various MSs with versatile functions have been presented to control the polarized states of EM waves, such as linear to linear polarization MSs [19–24], linear to circular polarization MSs [25], and circular to linear polarization MSs [26].

Asymmetric transmission (AT), a distinctive transmission phenomenon of EM waves, has been realized using a two-dimensional chiral structure in 2006. The conception of AT is described as the total transmission difference between reverse propagation directions, which is substantially triggered by the diverse polarization conversion capacities of media to two polarized waves orthogonal to each other [27]. AT refers to the phenomenon that different transmission results are obtained when the EM waves traverse the same medium in different directions. Just like the electronic diode feature, the current is only enabled to pass in a specific

Xiongwei Ma, Huanhuan Gao, and Linyan Guo contributed equally to this work.

✉ Xiaojun Huang
hxj@xust.edu.cn

✉ Xiaoyan Li
lixiaoyan0521@mail.nwpu.edu.cn

Xiongwei Ma
mxw.1998@qq.com

Huanhuan Gao
ghh1998kyjy@163.com

Linyan Guo
guoly@cugb.edu.cn

¹ College of Communication and Information Engineering, Xi'an University of Science and Technology, Xi'an 710054, China

² School of Geophysics and Information Technology, China University of Geosciences, Beijing 100083, China

³ College of Physical Science and Technology, Northwestern Polytechnical University, Xi'an 710072, China

direction, and the opposite direction is cut off [28]. As a special phenomenon in EM wave propagation, AT has an important application in polarization control, photodiode, and other fields, which has attracted widespread attention [29–32]. Many AT devices based on MS have been proposed, and the linear polarizer with cross-asymmetric transmission is one of the most common polarization devices [33]. A typical single-layer open ring resonator composed of two sets of gold is designed to realize asymmetric transmission and high-efficiency polarization conversion [34]. A bilayer split-ring transmitted polarizer with the AT parameter of 0.9 and polarization conversion ratio (PCR) of 93% at 12.7–17 GHz [35]. A triple layers polarizer designed using the genetic algorithm can achieve perfect reflection with the reflectance of 0.9 for y-polarized waves and high-effective cross-polarization transmission with the transmittance of 0.8 for x-polarized waves at 5.3–16.7 GHz [36]. However, many linear polarizers with good performance and asymmetric transmission have been proposed, higher PCR and wider RB are always our goals for such polarizers in actual applications.

In this paper, we propose an ultra-broadband polarizer similar to Fabry–Perot Cavity, which has a good ability for ultra-wideband efficient linear polarization in the microwave band. At 4.6–14.0 GHz, PCR is greater than 0.9 with the RB of 101.1%. We analyze multi-resonance, distributions of surface current and electric field to explore the physical characteristics of broadband, asymmetric transmission and polarization conversion. The measurements are inconsistent with the simulations satisfactorily, which further verifies our simulation results. We believe that our work is of great significance to potential applications for manipulating electromagnetic waves.

2 Basic theory

Herein, we assume that a plane structure is in the x - y plane, and a linearly electromagnetic wave is incident perpendicularly along the $+z$ -axis, the incident electric field is represented as:

$$\mathbf{E}^{in}(\mathbf{r}, t) = \begin{pmatrix} I_x \\ I_y \end{pmatrix} e^{j(-kz+\omega t)} \tag{1}$$

The transmission electric field is expressed as:

$$\mathbf{E}^{tr}(\mathbf{r}, t) = \begin{pmatrix} T_x \\ T_y \end{pmatrix} e^{j(-kz+\omega t)} \tag{2}$$

where I_x , I_y , T_x and T_y are the electric field component of the incident and transmissive waves on the x - and y -axis, separately.

The connection of electric fields between the incident and transmitted waves is depicted as:

$$\mathbf{E}_i^{tr} = t_{ij} \mathbf{E}_j^{in} \tag{3}$$

where i and j severally express x - and y -polarized states of electromagnetic waves. Thus, the relationship between the incident and transmitted waves is as follows:

$$\begin{pmatrix} E_x^{tr} \\ E_y^{tr} \end{pmatrix} = \begin{pmatrix} t_{xx} & t_{xy} \\ t_{yx} & t_{yy} \end{pmatrix} \begin{pmatrix} E_x^{in} \\ E_y^{in} \end{pmatrix} = \mathbf{T} \begin{pmatrix} E_x^{in} \\ E_y^{in} \end{pmatrix} \tag{4}$$

Jones matrix \mathbf{T} of the wave travels in the $+z$ -axis with the following formulas:

$$\mathbf{T}_{lin}^+ = \begin{pmatrix} t_{xx} & t_{xy} \\ t_{yx} & t_{yy} \end{pmatrix} \tag{5}$$

where t_{xx} and t_{yy} represent the co-polarized transmission parameters, t_{xy} and t_{yx} denote the cross-polarized transmission parameters. Based on the reciprocity theorem, when the electromagnetic wave is propagated in the $-z$ -direction, the amplitudes of t_{xy} and t_{yx} in Eq. (5) are exchanged and produced a phase shift of π . Then the transmission matrix changes are described as:

$$\mathbf{T}_{lin}^- = \begin{pmatrix} t_{xx} & -t_{xy} \\ -t_{yx} & t_{yy} \end{pmatrix} \tag{6}$$

According to margins between \mathbf{T}_{lin}^+ and \mathbf{T}_{lin}^- in Eqs. (5) and (6), the asymmetric transmission parameter Δ can express the strength of asymmetric transmission characteristics, and we define Δ as follows:

$$\Delta = |t_{yx}|^2 - |t_{xy}|^2 \tag{7}$$

The polarizers that generates the linearly polarized asymmetric transmission are satisfied as the following formula:

$$\Delta_{lin}^{(x)} = |t_{yx}|^2 - |t_{xy}|^2 = -\Delta_{lin}^{(y)} \tag{8}$$

where $\Delta_{lin}^{(x)}$ and $\Delta_{lin}^{(y)}$ correspond to the asymmetric transmission arguments of x -polarized and y -polarized, separately.

3 Design, simulation and experiments

The perspective and forward-looking of the designed polarization converter are illustrated in Fig. 1a, b. The upper and lower layers of the polarizer are mutually perpendicular gratings separated by the middle SRR layer at a 45-degree angle to the x -direction. The grating and SRR are made of copper, and the substrate is made of FR4 with relative permittivity of 4.3 and loss tangent of 0.025. The optimized geometries of structure are $a = 0.5$ mm, $b =$

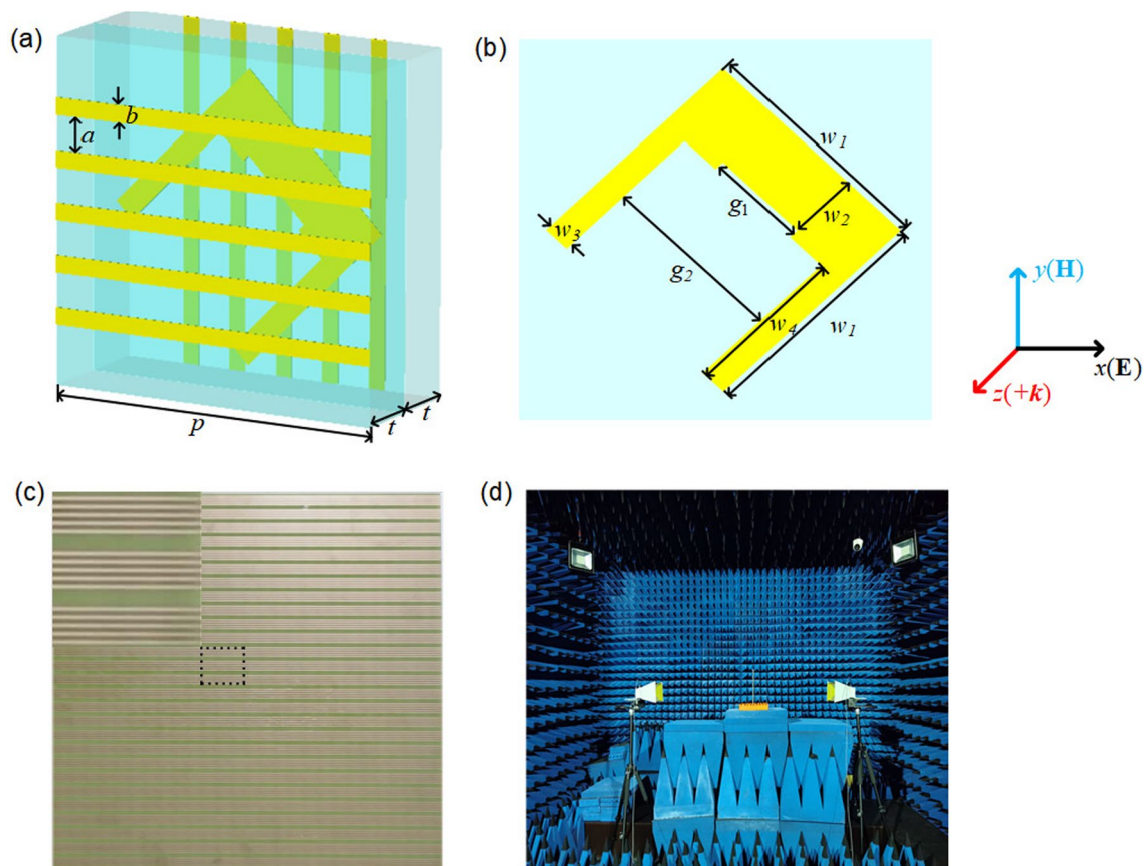


Fig. 1 Designed MS. **a** perspective view; **b** front view of SRR; **c** picture of the sample; **d** experimental environment

1.0 mm, $w_1 = 6.0$ mm, $w_2 = 1.75$ mm, $w_3 = 0.7$ mm, $w_4 = 4.0$ mm, $p = 10.0$ mm, $g_1 = 2.5$ mm, $g_2 = 4.6$ mm, $t = 2.0$ mm.

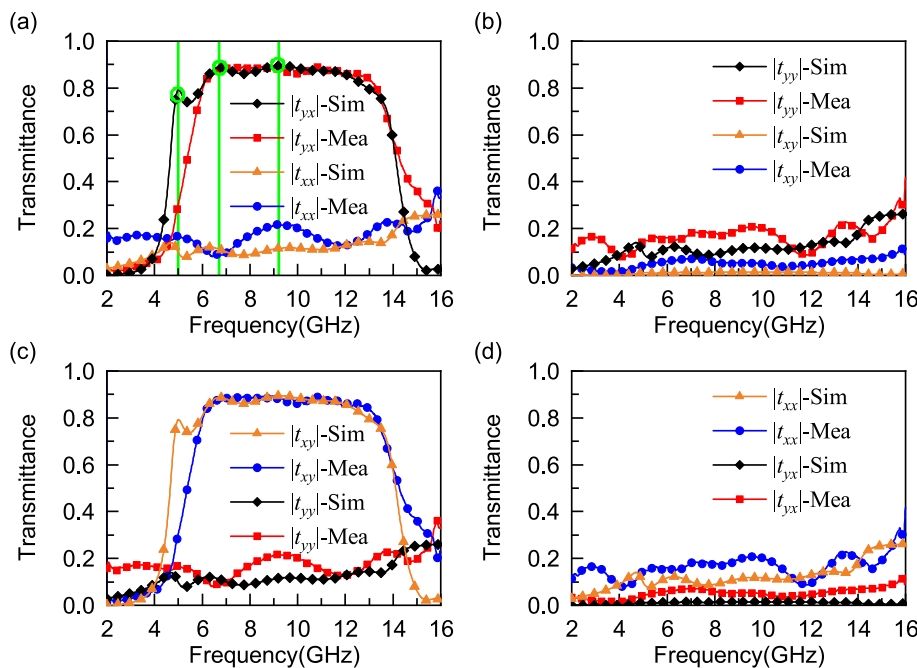
In the simulation, we use CST Microwave Studio to carry out the simulation using the frequency domain solver and define the linear polarization waves propagated in the $+z$ direction as the forward incident and the reverse incident in the opposite direction. Set the boundary conditions in x and y orientations as unit cell, and the boundary condition in z orientation as open add space. The forward incidence of the x - and y -polarized waves within 2–16 GHz is numerically simulated and the transmittances are extracted to obtain the four parameters of the transmission matrix. Figure 1c shows the experimental sample with the same geometry as the simulated structure in the experiment, and the experimental example is tested in the microwave anechoic chamber using the free space method, as shown in Fig. 1d. Our experimental devices have two horn antennas with 2–18 GHz bandwidth, which are used as transmitter and receiver concatenated with a vector network analyzer, respectively. The experimental sample is placed at a position about 75 cm away from the two horn antennas, and EM wave polarization states are adjusted by rotating the direction of the horn

antennas for testing the forward and backward co- and cross-polarization transmittances.

4 Results and discussion

The simulated and experimental results under the x - and y -polarized incident waves are depicted in Fig. 2. Figure 2a shows the cross-polarization transmittance t_{yx} under the x -polarized wave traveling in forward incident direction is larger than 0.8, while the co-polarization transmittance t_{xx} is less than 0.2 at 4.3–13.7 GHz. Figure 2b describes that the co-polarized transmittance t_{yy} and the cross-polarized transmittance t_{xy} of the y -polarized wave propagating along the $+z$ -axis are less than 0.2. This result indicates that when the x -polarized wave propagates along forward direction, the wave passes through the MS and converts into its orthogonal polarized wave, while the y -polarized wave traveling in the same direction is blocked instead of passing through the MS. Furthermore, when the same procedures are carried out to the y -polarized wave spreads along reverse incident direction, we find that the y -polarized wave has the same performance as the x -polarized wave traveling along $+z$ -axis. This

Fig. 2 The transmittances in forward direction (+z). **a** x-polarization; **b** y-polarization. the transmittances in backward direction (-z). **c** y-polarization; **d** x-polarization



confirms that proposed MS can realize efficient asymmetric transmission of electromagnetic waves.

Figure 3 shows the simulated and experimental polarization conversion ratio (PCR) as the *x*- and *y*-polarized waves travel on the *z*-axis. Figure 3a depicts the PCR under the *x*-polarized incident wave propagating along the +*z*-axis, which value is greater than 0.9 at 4.6–14 GHz, while the PCR under the *y*-polarized wave is less than 0.2 in same region. This phenomenon suggests that the *x*-polarized wave is cross-polarized and turns into *y*-polarized state after penetrating through the MS in this frequency range, while the *y*-polarized wave is transmitted as co-polarization without polarization conversion. When the EM wave travels on the -*z*-axis, the effect is exactly the opposite of the effect in the +*z* direction. It should be noted that the measured PCR band in Fig. 3 is wider than the simulated band. This discrepancy can be attributed to a lack of processing accuracy and differences in material parameters during processing and simulation. Additionally, since the simulation assumes an

infinite boundary, but the sample is a finite plane, electromagnetic edge diffraction is also likely to play a role in the discrepancy between the simulated and measured results. Form Fig. 4, we calculate the asymmetric parameters. Figure 4a shows that when the linear EM wave propagates along the +*z* direction, the asymmetric parameters are greater than 0.8 and less than -0.8 at 6.0–12.9 GHz. When the EM wave travels in -*z* direction, the asymmetric parameters are less than -0.8 and greater than 0.8, respectively. The above results verify that the designed MS realizes broadband polarization conversion and asymmetric transmission.

The following section investigates the influence of the geometry of the polarizer on the PCR using *x*-polarized waves as the incident source in the +*z*-axis. The size of the polarizer period and the thickness of the dielectric layer play an important role in the phase change of the electromagnetic wave during propagation and thus in the polarization conversion performance of the polarizer. To analyze the polarization performance of the polarizer, the geometric parameters

Fig. 3 PCR. **a** Forward direction (+z); **b** backward direction (-z)

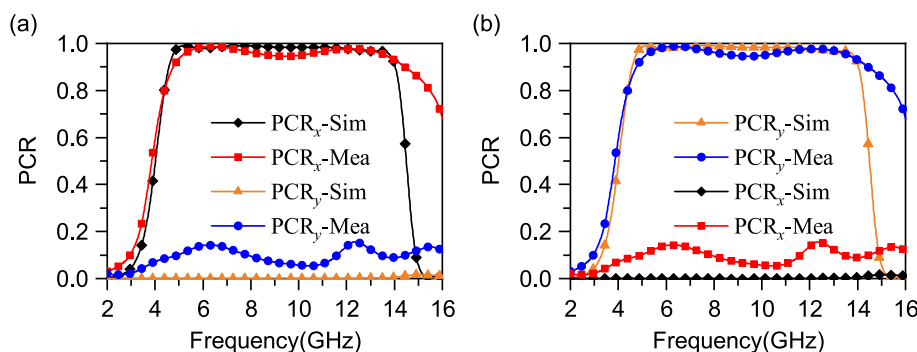
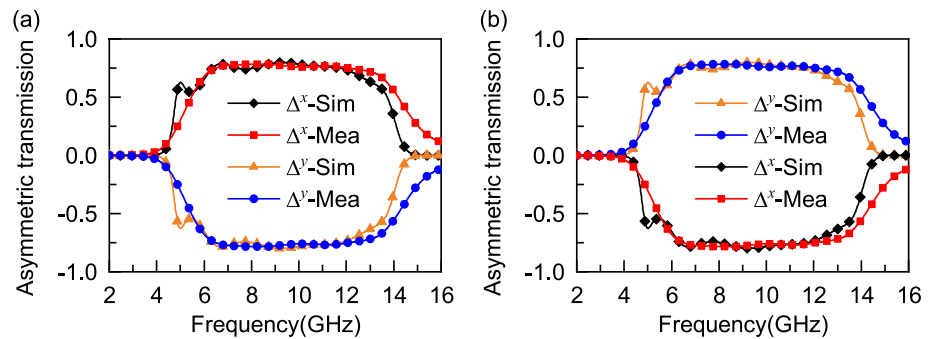


Fig. 4 Asymmetric transmission **a** forward direction (+z); **b** backward direction (-z)

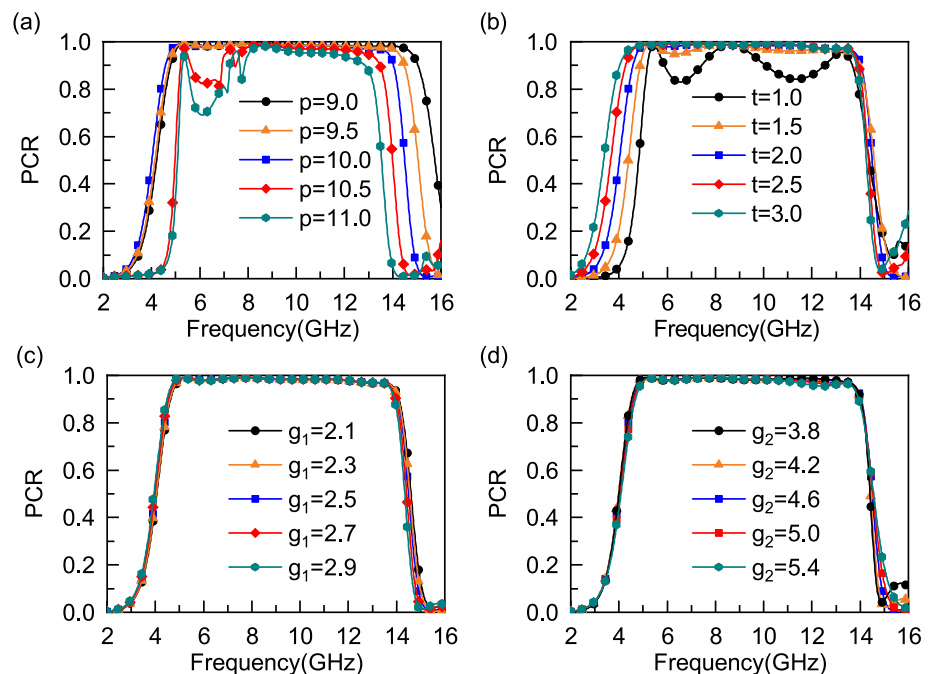


of the period (p), dielectric thickness (t), and the size of the split-ring resonator (g_1 and g_2) were optimized. Figure 5a shows the effect of varying the period p from 9 to 11.0 mm on PCR. As the p decreases from 11 to 9 mm, the entire bandwidth of the polarization conversion undergoes redshift and blueshift. The increase in bandwidth shows a nonlinear relationship in the low-frequency range of 2–4 GHz, while the increase in bandwidth shows a linear broadening in the high-frequency range of 13–16 GHz. This is due to the smaller resonant structure size resulting from the decrease in period, leading to an increased operating bandwidth. Additionally, the decrease in p leads to an improvement in PCR, reaching 0.99 in the frequency range of 6–8 GHz. This is because the coupling resonance of adjacent cells is enhanced as the cell structure becomes smaller, resulting in a significant change in PCR. Figure 5b shows the effect of varying the t from 1 to 3 mm on PCR. There is a clear linear redshift in the low frequency range of 2–4 GHz with increasing thickness, and PCR also gradually increases to above 0.99.

This is because an increase in thickness enhances the resonance within the resonant cavity of the multilayer structure, resulting in a shift to lower frequencies and a significant change in the phase of the electromagnetic wave. Finally, the influence of the gaps (g_1 and g_2) on PCR was analyzed, and Fig. 5c, d show that neither g_1 nor g_2 has a significant impact on PCR. These analyses of the parameters provide important guidelines for parameter optimization.

Generally, multilayer metasurfaces are capable of providing a broad bandwidth of polarization conversion and asymmetric transmission, due to the presence of the Fabry–Perot resonance between the two metal layers. This resonance enhances the polarization conversion and asymmetric transmission performance of the structure [37]. However, a single layer of high-Q resonator metasurface can only achieve narrowband or multi-band polarization conversion and asymmetric transmission. As described in Fig. 6, when the x - and y -polarized waves are incident to polarizer in +z direction, the x -polarized wave penetrates through the top

Fig. 5 PCR under different geometric parameters. **a** p ; **b** t ; **c** g_1 and **d** g_2



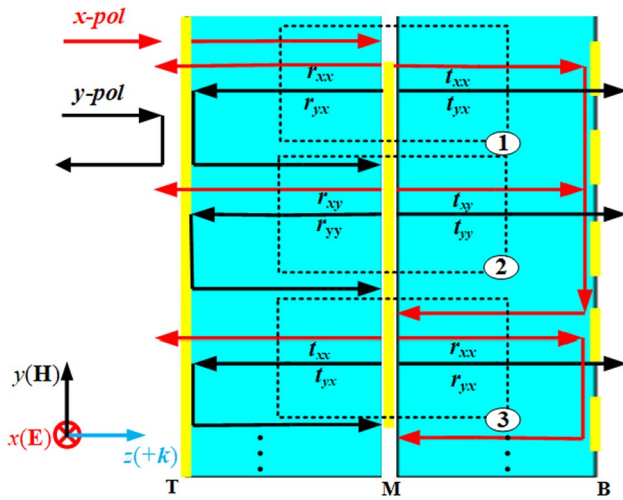


Fig. 6 Fabry-Perot-like resonance in multi-metallic layers

layer (T) while the y-polarized wave is directly reflected in form of co-polarized wave due to the selective transmittance of the grating. The x-polarized wave is propagating directly through top layer and arriving at the middle layer (M), and be reflected and transmitted in form of the co-polarization

and cross-polarization (r_{xx} , r_{yx} , t_{xx} , t_{yx}) under the action of SRR on the middle layer, as shown in the dashed area 1 of Fig. 6. For the reflection, the reflected x-polarized wave (r_{xx}) penetrates through top layer (T) whereas the y-polarized wave (r_{yx}) is reflected as co-polarization from the top layer (T) and reaches the middle layer (M). For the transmission, the cross-polarized transmission wave in form of y-polarized (t_{yx}) directly passes through the bottom layer (B), but the co-polarized transmission wave in form of the x-polarized (t_{xx}) is given back from the bottom layer (B).

In dashed area 2, the y-polarized wave, from the reflected wave in dashed area 1, can also be subdivided into four components (r_{yy} , r_{xy} , t_{yy} , t_{xy}). The cross-polarized wave (r_{xy}) is reflected to the top layer and the transmitted wave (t_{yy}) in form of co-polarized penetrates the bottom layer. Conversely, the co-polarized reflected wave (r_{yy}) and cross-polarized transmitted wave (t_{xy}) continue to follow the propagation stated above, as shown in dashed area 3. Therefore, the bandwidth is enhanced and extended except for polarization conversion after the constantly reflected and transmitted incident EM wave in the resonant-cavity-like polarizer.

As indicated in Fig. 7, we illustrate the surface current distributions at two resonant points to expose the physics of asymmetric transmission and polarization conversion. The

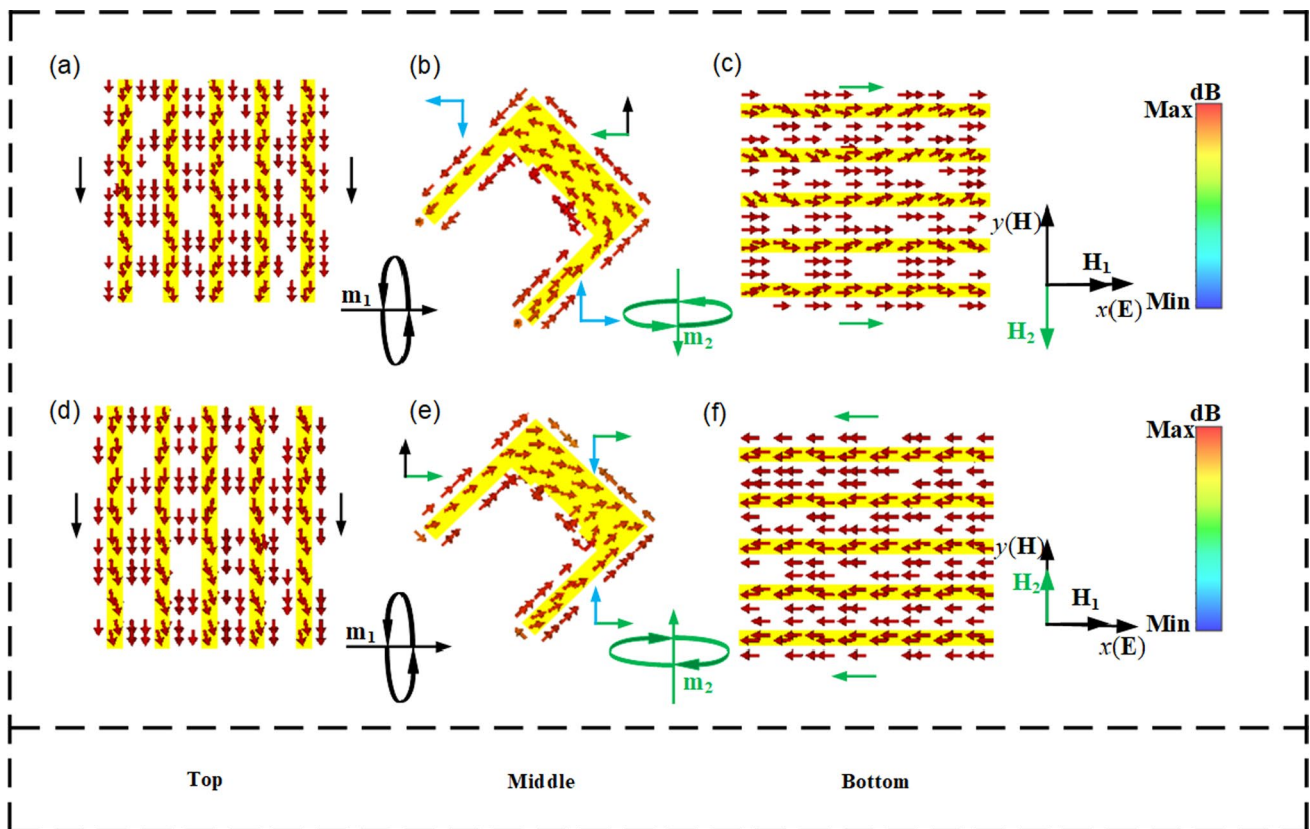
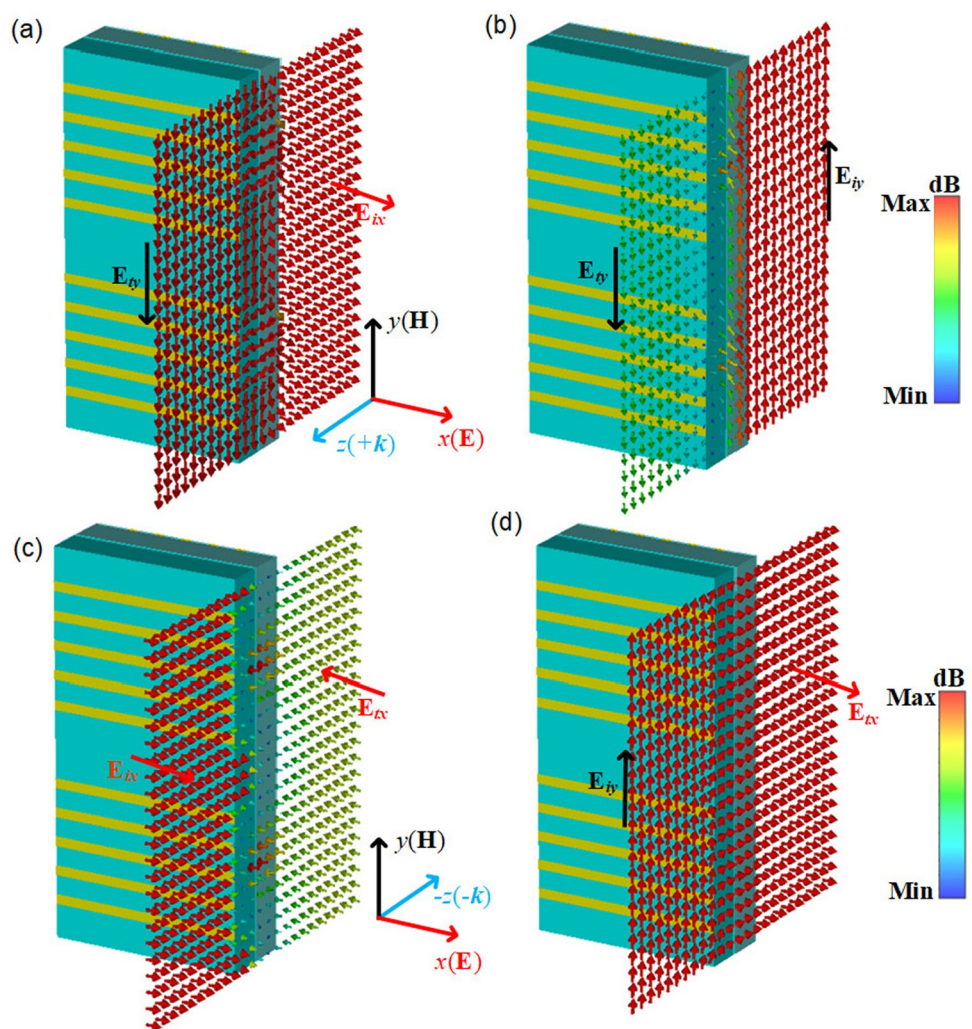


Fig. 7 Surface current distributions of the x-polarized wave in +z-axis. a–c 5.0 GHz; d–f 6.7 GHz

Fig. 8 The electric field distribution in $+z$ -axis at 6.7 GHz. **a** x -polarized; **b** y -polarized; the electric field distribution in $-z$ -axis at 9.2 GHz. **c** x -polarized; **d** y -polarized



surface current distribution under the x -polarized illuminating along $+z$ -axis at 5.0 GHz is described in Fig. 7a–c, which observes clearly that the top and bottom gratings surface currents are distributed along the grating direction, and the surface currents on the middle layer are dissolved on the x - and y -directions. The surface currents decomposed in the y direction are parallel and opposite to the surface currents on the top grating, which form a magnetic dipole \mathbf{m}_1 (black arrow) along the x direction and corresponding magnetic fields \mathbf{H}_1 in the x direction. Furthermore, the currents on the middle layer decomposed in the x -axis parallel the currents at the bottom of the grating in the opposite direction, this creates a magnetic dipole \mathbf{m}_2 (green arrow) along the y direction. The magnetic dipole \mathbf{m}_2 is generated in the y direction, and the corresponding electric field is on x -axis, which illustrates the transmitted wave is y -polarized. Similarly, Fig. 7d–f also have the same polarization conversion physics. On the top layer currents and the x -direction component of the middle layer currents form the magnetic dipole \mathbf{m}_1 , on the middle layer currents of the y -axis component and the surface currents on the bottom layer

form the magnetic dipole \mathbf{m}_2 . The blue arrows indicate the equal but opposite currents on the SRR layer, which cancel each other out.

We also illustrate the distribution of the electric fields at 6.7 and 9.2 GHz. From Fig. 8a, the x -polarized wave traveling along the $+z$ -axis is transformed into y -polarized state at 6.7 GHz. It can be seen from Fig. 8b that the transmission electric field is extremely weak under the y -polarized wave propagating along the $+z$ -axis, which manifests that y -polarized is obstructed instead of passing through. When the x -polarized is traveled on $-z$ -axis at 9.2 GHz, as depicted in Fig. 8c, the transmission features are exactly reverse of the $+z$ direction, which can be concluded that most of the x -polarized waves are reflected in co-polarization state. Similarly, the y -polarized wave propagated along the $-z$ -axis is transformed perfectly into the x -polarized, as illustrated in Fig. 8d. These results once again directly show that the designed polarizer strictly realizes asymmetric transmission.

Finally, to showcase the superiority of the design, we compare the proposed asymmetric transmission polarizer with

Table 1 Comparison with recently published works

Ref	PCR (%)	OB (GHz)	RB (%)	Thickness (mm)	Structure
[35]	90	12.7–17.0	30.0	1.5	Single
[38]	80	8.0–9.1	13.0	2.1	Single
[39]	80	8.1–9.3	13.8	1.2	Single
[36]	80	5.3–16.7	103.6	5.0	Multilayer
[40]	80	12.0–18.0	40.0	2.4	Multilayer
[41]	80	6.3–12.3	64.0	2.3	Multilayer
This work	90	4.6–14.0	101.0	4.0	Multilayer

OB operating bandwidth; RB relative bandwidth

other recent works, as shown in Table 1. The results demonstrate that the proposed MS has a wide bandwidth and excellent polarization performance, outperforming other designs in both the C- and X-bands. The single-layer MS in literature [35] has a high PCR of 0.9 and a thickness of only 1.5 mm, but its performance is limited to a narrowband. MSs in literature [38] and [39] are also relatively thin, but they are still restricted to narrowband operation. The multilayer MS in literature [36] has a relative bandwidth of up to 103.6%, but it has a lower PCR of 0.8 and a thickness of 5 mm. The MSs in literature [40] and [41] also have smaller thicknesses, but their PCR is slightly lower. Compared to these works, our proposed MS offers a more comprehensive solution.

5 Conclusion

To sum up, we have proposed a wideband linear polarizer using a three-layers MS with abilities of high-efficient polarization conversion and asymmetric transmission, which PCR is greater than 0.9 at 4.6–14.0 GHz with a wideband asymmetric transmission, and the asymmetry coefficients achieve 0.8 at 6.0–12.9 GHz. Microwave experiment results are consistent with our simulations. The Fabry–Perot cavity resonance is introduced to explore the principle of increasing broadband. The asymmetric transmission and polarization conversion performance are further verified by analyzing distributions of surface current and electric field. Our polarizer has the advantages of simple structure and certain performance advantages, which has a wide application expectation in polarization conversion, photodiode, electronic communication, and other fields.

Acknowledgements This work was supported by the National Natural Science Foundation of China (No. 42274189) and the Project of Science and Technology of Shaanxi (2021JM-395).

Declarations

Conflict of interest The authors have no competing interests to declare that are relevant to the content of this article.

References

1. C.L. Holloway, An overview of the theory and applications of metasurfaces: the two-dimensional equivalents of metamaterials. *IEEE Antennas Propag. Mag.* **54**, 10–35 (2012)
2. X. Huang, Ultrathin dual-band metasurface polarization converter. *IEEE Trans. Antennas Propag.* **67**, 4636–4641 (2019)
3. T. Shibanuma, Polarization control of high transmission/reflection switching by all-dielectric metasurfaces. *Appl. Phys. Lett.* **112**, 063103 (2018)
4. J. Yang, Simultaneous conversion of polarization and frequency via time-division-multiplexing metasurfaces. *Adv. Opt. Mater.* **9**, 218–227 (2021)
5. Q. Zheng, Efficient orbital angular momentum vortex beam generation by generalized coding metasurface. *Appl. Phys. A Mater. Sci. Process.* **125**, 136 (2019)
6. A.M.H. Wong, Perfect anomalous reflection with a bipartite Huygens' metasurface. *Phys. Rev. X* **8**, 011036 (2018)
7. H.-H. Hsiao, Fundamentals and applications of metasurfaces. *Small Methods* **1**, 1600064 (2017)
8. A. Li, Metasurfaces and their applications. *Nanophotonics* **7**, 989–1011 (2018)
9. F. Ding, Gradient metasurfaces: a review of fundamentals and applications. *Rep. Prog. Phys.* **81**, 026401 (2018)
10. Y. Ge, Broadband folded transmitarray antenna based on an ultrathin transmission polarizer. *IEEE Trans. Antennas Propag.* **66**, 5974–5981 (2018)
11. Q. Song, Water-resonator-based metasurface: an ultrabroadband and near-unity absorption. *Adv. Opt. Mater.* **5**, 1601103 (2017)
12. X. Wang, Metal-free oxide-nitride heterostructure as a tunable hyperbolic metamaterial platform. *Nano Lett.* **20**, 6614–6622 (2020)
13. F. Zhang, All-dielectric metasurfaces for simultaneous giant circular asymmetric transmission and wavefront shaping based on asymmetric photonic spin–orbit interactions. *Adv. Funct. Mater.* **27**, 1704295 (2012)
14. H. Wang, A circular-polarized metasurface planar reflector antenna based on Pancharatnam-Berry phase. *Sci. Process.* **125**, 274 (2019)
15. W. Sun, A transparent metamaterial to manipulate electromagnetic wave polarizations. *Opt. Lett.* **36**, 927 (2011)
16. X. Huang, Simultaneous realization of polarization conversion for reflected and transmitted waves with bi-functional metasurface. *Sci. Rep.* **12**, 2368 (2022)
17. M.R. Akram, Ultrathin single layer metasurfaces with ultrawideband operation for both transmission and reflection. *Adv. Mater.* **32**, 1907308 (2020)
18. L.W. Wu, Transmission-reflection controls and polarization controls of electromagnetic holograms by a reconfigurable anisotropic digital coding metasurface. *Adv. Opt. Mater.* **8**, 2001065 (2020)
19. S. Gao, Efficient all-dielectric diatomic metasurface for linear polarization generation and 1-Bit phase control. *ACS Appl. Mater.* **13**, 14497–14506 (2021)
20. F. Ding, Gap-surface plasmon metasurfaces for linear-polarization conversion, focusing, and beam splitting. *Photonics Res.* **8**, 707 (2020)

21. P. Science, Ultra-broadband wide-angle linear polarization converter based on H-shaped metasurface. *Opt. Express* **26**, 20913–20919 (2018)
22. X. Yang, Broadband linear polarization conversion across complete Ku band based on ultrathin metasurface. *AEU Int. J. Electron. Commun.* **138**, 153884 (2021)
23. Z. Liu, Broadband cross-polarization conversion metasurface based on cross-shaped resonators. *Appl. Phys. A Mater. Sci. Process.* **127**, 825 (2011)
24. Z. Liu, Design of broadband transmission polarization conversion metasurface based on cross-shaped resonators. *Appl. Phys. A Mater. Sci. Process.* **128**, 681 (2022)
25. B. Lin, Design of a wideband transmissive linear-to-circular polarization converter based on a metasurface. *Appl. Phys. A Mater. Sci. Process.* **124**, 715 (2018)
26. J.T. Heiden, Gap-surface plasmon metasurfaces for broadband circular-to-linear polarization conversion and vector vortex beam generation. *Adv. Opt. Mater.* **7**, 1801414 (2019)
27. V.A. Fedotov, Asymmetric propagation of electromagnetic waves through a planar chiral structure. *Phys. Rev. Lett.* **97**, 167401 (2006)
28. M. Mutlu, Diodelike asymmetric transmission of linearly polarized waves using magnetoelectric coupling and electromagnetic wave tunneling. *Phys. Rev. Lett.* **108**, 213905 (2012)
29. M. Feng, Ultra-wideband and high-efficiency transparent coding metasurface. *Appl. Phys. A Mater. Sci. Process.* **124**, 630 (2018)
30. M. Kim, A broadband optical diode for linearly polarized light using symmetry-breaking metamaterials. *Adv. Opt. Mater.* **5**, 1700600 (2017)
31. E.B. Whiting, Broadband asymmetric transmission of linearly polarized mid-infrared light based on quasi-3D metamaterials. *Adv. Funct. Mater.* **32**, 2109659 (2022)
32. J. Li, Active controllable spin-selective terahertz asymmetric transmission based on all-silicon metasurfaces. *Appl. Phys. Lett.* **118**, 221110 (2021)
33. P. Fei, Cross-polarization conversion chiral metasurface for linear and circular polarizations. *Adv. Opt. Mater.* **8**, 2000194 (2020)
34. Z. Li, Manipulation of asymmetric transmission in planar chiral nanostructures by anisotropic loss. *Adv. Opt. Mater.* **1**, 482–488 (2013)
35. F. Long, Wideband and high-efficiency planar chiral structure design for asymmetric transmission and linear polarization conversion. *J. Appl. Phys.* **127**, 023104 (2020)
36. W. Ji, High-efficiency and ultra-broadband asymmetric transmission metasurface based on topologically coding optimization method. *Opt. Express* **27**, 2844–2854 (2019)
37. Y. Wang, Enhanced asymmetric transmissions attributed to the cavity coupling hybrid resonance in a continuous omega-shaped metamaterial. *Opt. Express* **26**, 3508–3517 (2018)
38. P. Xu, An ultrathin cross-polarization converter with near unity efficiency for transmitted waves. *IEEE Trans. Antennas Propag.* **8**, 4370–4373 (2018)
39. S.H.A. Bokhari, A bi-layered, broadband, angularly robust chiral metasurface for asymmetric transmission. *IEEE Antennas Wirel. Propag. Lett.* **1**, 23–27 (2021)
40. Z. Xiao, Multi-band transmissions of chiral metamaterials based on Fabry–Perot like resonators. *Opt. Express* **354**, 272–276 (2015)
41. S.H.A. Bokhari, Ultra-wideband, wide angle, asymmetric transmission based chiral metasurface for C and X band applications. *Sci. Rep.* **1**, 11724 (2021)

Publisher's Note Springer Nature remains neutral with regard to jurisdictional claims in published maps and institutional affiliations.

Springer Nature or its licensor (e.g. a society or other partner) holds exclusive rights to this article under a publishing agreement with the author(s) or other rightsholder(s); author self-archiving of the accepted manuscript version of this article is solely governed by the terms of such publishing agreement and applicable law.